

Real-time optical space situational awareness of low-Earth orbit with small telescopes

Peter Zimmer

J.T. McGraw and Associates, LLC

John T. McGraw

J.T. McGraw and Associates, LLC

Mark R. Ackermann

J.T. McGraw and Associates, LLC

ABSTRACT

Small optical systems are poised to contribute substantial, robust measurements of low-Earth orbit (LEO) objects for ground-based space situational awareness (SSA), detecting new objects and monitoring known ones. The physics of these observations is sufficiently different from, and complementary to, the radar systems that have long been the dominant provider of data in this regime.

Numerous constellations of small LEO satellites have been announced for launch in the next few years. If even a fraction these are deployed, the LEO orbital regime will become even more crowded than it already is, with strategic, logistical and economic impacts. Cost-effective optical systems optimized for LEO detection can help address the resulting challenges posed by these constellations. Widely deployed, these optical systems can overcome the inherent limitations of ground-based optical telescopes, primarily weather and Sun-illumination conditions, creating a rich, new, cost-effective data source.

We've previously demonstrated that small, commercial-off-the-shelf (COTS) derived optical systems can detect and measure, in real-time, LEO objects smaller than 10 cm. We discuss recent improvements to our fielded optical systems and demonstrate performance as a function of object size and range.

1. INTRODUCTION

The wise stewardship of Earth's orbital volume demands precise and accurate surveillance of space at a rapid cadence with coverage as complete as practical reality allows. No one system or technology is sufficient; complementary tools and techniques are necessary. There is an analogy in fundamental physics: The world's most accurate clock is meaningless without the world's second most accurate clock. Repeatability of inherently different measurements gives true confidence in one's model of reality. And the dynamic nature of Earth's orbital volume requires robust models to understand and predict its current and future states. To ensure this diversity of measurement, alternatives to optical measurements of geostationary objects are needed, such as large dish radar [1], [2] and passive radio frequency detectors [3]. Alternatives to radar for LEO surveillance are also needed, including, but not limited to, passive optical measurements such as those shown here.

Optical telescopes are most frequently used for monitoring geostationary objects. Many objects in this orbital regime can be easily monitored because their apparent angular rate is relatively slow, minimizing the signal-to-reduction caused by trailing loss[4]. Compromises between exposure time on the object and maintaining measurable star images balance the competing effects of greater sensitivity versus better photometry and astrometry. Standard astronomical analysis techniques can be adapted to properly measure images in these circumstances, because the objects still resemble point-spread functions and calibration against known catalog stars is still practical.

The conditions under which more traditional astronomical techniques excel in detecting and accurately measuring objects in orbit are essentially dictated by the objects' apparent angular rate. Objects in geostationary equatorial orbits (GEO) have very small apparent angular rates, especially when observed from the Earth's nearly co-rotating surface, and those that are near it also have similarly small rates, typically in the range of a few tens of arcseconds per second. Medium Earth orbit (MEO) objects typically show rates a few tens to a few hundred arcsecond per second, with objects such as GPS satellites having apparent angular rates of roughly 40 arcseconds per second. For all but the lowest portion of this regime, the canonical techniques can still yield reliable results if short enough

exposure times can be implemented to confine the motion to relatively short streaks. Depending upon the telescope system used, the detection limit may be hit due to mechanical or electronic factors, or for small telescopes, there simply may not be enough signal captured in a short exposure to measure either the object or the stars effectively. Also, short exposures can lower the overall system throughput drastically if they are much shorter than any deadtime between exposures. These issues can be encountered whether the system is rate-, sidereal-, or fixed-tracking an object, though in the case of rate-tracking faster moving objects, one quickly loses the ability to accurately measure background stars critical for calibration.

There then exists a transition point where point-source measurements are superseded by streak detection and measurement if one wishes to use stars for contemporaneous calibration. The authors have previously presented work covering measurements on both sides of this transition [5]–[8]. These works have covered measurements of objects all throughout LEO, MEO, and GEO.

2. CUED OBSERVATIONS OF LEO OBJECTS

Our previous work measuring objects in LEO has focused on uncued/blind detection of objects [9]. Optical images appropriately obtained can be searched, looking for objects moving at high angular rates that cause streaks. Brute force streak detection techniques are effective but computationally intense. The detection intensity threshold can be lowered significantly when modified for cued observing. Expected rates and locations can be used to narrow the search space, allowing rapid detection and measurement of even faint objects.

Cued observations are very much the yeoman’s work of SSA. Objects are probably very close to the published catalog position, but the uncertainties of orbit propagation, as well as known and unknown maneuvers or accidents, make the cases in which things aren’t where they should be quite interesting. Moreover, very little is known about the optical properties of the very small debris objects that make up the bulk of the current public catalog.

2.1. Using Small Optical Telescopes for Cued SSA of LEO

There are numerous practical challenges involved in using optical telescopes to observe LEO objects. The objects themselves are fairly bright as astronomical sources, where even the reflected light from a golf ball at 1000 km distance is around 14th magnitude, a value 1600 times fainter than is observable with the naked eye, but an easy target for small telescopes. That corresponds to hundreds, if not thousands, of photons per second for small telescopes — a great plenty, if the target isn’t moving fast. Objects in LEO orbits appear to move several hundred to several thousand arcseconds per second, which smears that generous signal across a great many detection elements and does not allow the signal to accumulate in a localized position.

Most optical LEO observations tend to be obtained with the optical system tracking the expected path, actively slewing the telescope to track it. This has the advantage of allowing the signal from the object to accumulate in a small area, minimizing noise contributions. In this mode, background stars smear out, reducing or eliminating them as calibration sources and turning them into a highly variable and difficult-to-model background. This presents two problems: Photon noise from stars is spread widely over the field of view (FOV), and systemic errors arise due to incomplete modelling and removing of the streaked star images.

JTMA personnel believe that stars are our friends, providing both an exquisite inertial coordinate reference and a precise, and reasonably fundamentally accurate radiometric calibration. Therefore, our approach is to point the system FOV ahead of the expected trajectory, tracking the sidereal rate, and acquire rapid, wide-field images while the object moves through. This results in stacks of images where the stars make small round images, confining their flux to a small number of pixels, and the LEO objects make streaks. At our typical frame rates, those streaks range from a few pixels to a few hundred pixels long.

2.2. The detection system

The underlying telescope system, as shown in Figure 1, is largely unchanged from our previous work. The optical system is a Celestron C-14 fitted with a Hyperstar prime-focus corrector, which operates at $f/1.9$ and delivers a $1.88^\circ \times 1.88^\circ$ field of view onto the GPixel GSense400BSI sensor. The $11\ \mu\text{m}$ pixels subtend $3.32''$ and have a measured median read noise of $1.8\ e^-$. The camera is thermoelectrically cooled to $-10\ \text{C}$, which is sufficient to make the dark current for most pixels negligible, and systematically high noise pixels are readily masked. The sensor is housed in a

Tucson Dhyana 95 camera operated via USB 3.0, which is required for the high data rate, which can exceed 100 megapixels per second.



Figure 1 – The 0.35m Optical SSA system used for this work is located in north central New Mexico.

2.3. The observations

We tasked the 0.35m system (see upper panel of Figure 1) to observe a largely *ad hoc* list of LEO objects that overflow our observing site in Placitas, NM during four twilight periods in Jan. 13-15, 2018. The telescope was commanded to “step ahead and stare” on the Space-Track.org TLE position. Thirty-two frames with 0.1s exposure time each are then obtained both before and after the expected crossing time. Slower moving objects start and end in the FOV, while faster moving objects will enter and exit the FOV during the dwell period. The telescope is then repositioned ahead of the object and the sequence is repeated until the object falls below a preset limit of 20 degrees elevation, or the telescope is tasked to a different object. In this mode, between two and five pointings can be made per minute, depending on the speed of the object. Switching objects can require longer slews and can add up to a minute of dead time. All told, we observed 51 objects in 250 pointings during the four clear twilights in the test observing period. Most of these observations were of large, bright active LEO satellites, but we paid particular attention to targeting some small cubesats and debris objects.

The obtained imagery was processed to remove instrumental signatures which are analogous to bias, dark and flat field frames in standard CCD astronomy, though these are modified for the sCMOS detector we used. The resulting frames are then reduced to GAIA DR2 [10], [11] positions and intensities. The system runs in a wide-open band without a filter which results in a spectral response similar to the GAIA g-band. Each frame measures several hundred to several thousand GAIA stars brighter than 16th magnitude, which allows a very consistent photometric and astrometric reference. The individual frames are short enough that scintillation places the ultimate limits on photometric and astrometric precision – for objects detected at a signal-to-noise (S/N) ratio greater than 20, we typically measure 7% to 10% photometric residuals and 0.25 arcsecond astrometric residuals in individual exposures. There is a strong field dependence, however, because of the significant (>50%) vignetting of the FOV inherent in the Hyperstar corrector between the center of the field and the corners. The objects in question necessarily cross the field, so that an object with a high S/N in the center may have a much-diluted detection at the edge. Each field contains a few thousand catalog stars, from 2,000 up to 14,000 when close to the galactic plane. Coordinates are fit with a high-order polynomial surface. Stars are then masked with an empirically derived function based on catalog star (and bright nebula, galaxy, and planet) positions.

The resulting 2048 x 2048 x 64-pixel data cubes are reduced by JTMA’s GPU-based object detection system. Because we are operating in cued mode, we use the expected rate to guide our detection and analysis pipeline, which

reduces the processing time dramatically and enables the use of much more limited computational systems. Objects that exceeded a threshold of six sigma of the expected noise were flagged for verification.

2.4. Photometric model estimates of satellite intensity.

To better understand the system performance and assess detection limits, we applied what has become the standard for intensity estimation of objects for which detailed information of size and shape are not known – we assume a diffusely scattering sphere [12]. Because we have knowledge of these objects' positions in advance, we can make good estimates of range and solar phase angle simply from the TLE positions. We use a slightly modified version of the equation first detailed in [13], adjusted for the GAIA magnitude for the Sun of -26.89 [14]:

$$m_{sat} = -26.89 + 2.5 * \log_{10} \left(\frac{\rho AF(\theta)}{R^2} \right)$$

where A is the projected area of the object, F(θ) is the scattering phase function at time of observation [13], ρ is the average albedo, and R is the range to the object. The phase angle and range are known. Because all the objects observed were first detected some years ago, in the cases where we don't have good *a priori* knowledge of the object, we can take measured radar cross sections (RCS) for each object using historical RCS data (from when such information was still routinely published for public catalog objects). Those cross sections can be converted into an *approximate* object size using the NASA SEM2 model [15], [16] that takes into account the various wave-scattering physics involved. This is important, because several of the objects measured fall below the region where geometric scattering is expected to occur for space surveillance radar, taken to have a wavelength of 0.68 m. In cases where the cross section falls between 0.014 m² and 1.0 m², the measured cross section is likely to have been an overestimate of the physical size because of Mie scattering and would estimate the object to appear brighter and thus a lower magnitude. When the RCS is below 0.014 m², Rayleigh scattering is the dominant mechanism, and the RCS is likely an underestimate of the physical size.

The remaining factor that must be estimated is albedo. Within the SSA community, a range of values is typically used as typical for debris from 10% to 18% [17]. Reality clearly offers a wide range of values. We pick for our model a value of 15.85%, because it is both oddly specific and represents closely two magnitudes of reduction from an albedo of 100%. And because our measurements are registered against measured GAIA magnitudes, we find this choice to be a handy reference point – calculate the expected magnitude for unity albedo and add two. This places some limits on interpretation of resulting measurements because objects with an intensity two magnitudes brighter than expected are either significantly larger than estimated or have a significant specular component to the reflectivity. Objects more than two magnitudes fainter also require some explanation. In addition, the unknown systematic errors between a simple model such as this are large enough that detailed choice of albedo is not worthwhile. Still a model such as this can guide our understanding and put measured values in a valuable context even if the specifics of the area-albedo product are not presently independently knowable.

3. INITIAL RESULTS

We present here the preliminary measurements of the objects observed along with their estimated intensity, both referenced to the GAIA photometric system. For the purposes of this report, we focus on the results from the objects we find most interesting: calibration satellites because they are well understood; cubesats because they are small and soon to be very numerous in LEO; and Fengyun-1C debris because it is really small and notoriously difficult to observe optically.

3.1. Calibration Objects

We specifically targeted three passes of radar calibration objects: LAGEOS 1 & 2 and CALSPHERE 2. A summary of these observations is shown in Table 1 at the end of this section. The LAGEOS satellites are 0.6-m diameter aluminum-covered brass spheres with 426 corner cube reflectors. Figure 2 shows a picture of LAGEOS 1, and Figure 3 shows a sample track, made up of a sum of every-other image from one of the image sets to show the frame to frame and overall behavior. The LAGEOS satellites are in 6000 km altitude MEO orbits, hence the very short per-frame streak, but compared to most objects in orbit, have a relatively simple and well-understood shape. Because we know the physical size of these satellites, and they are spheres, there is no need to invoke the RCS, and we can calculate the area directly. It's worth noting that the geometrical area of 0.28 m² is about 30% lower than the RCS.

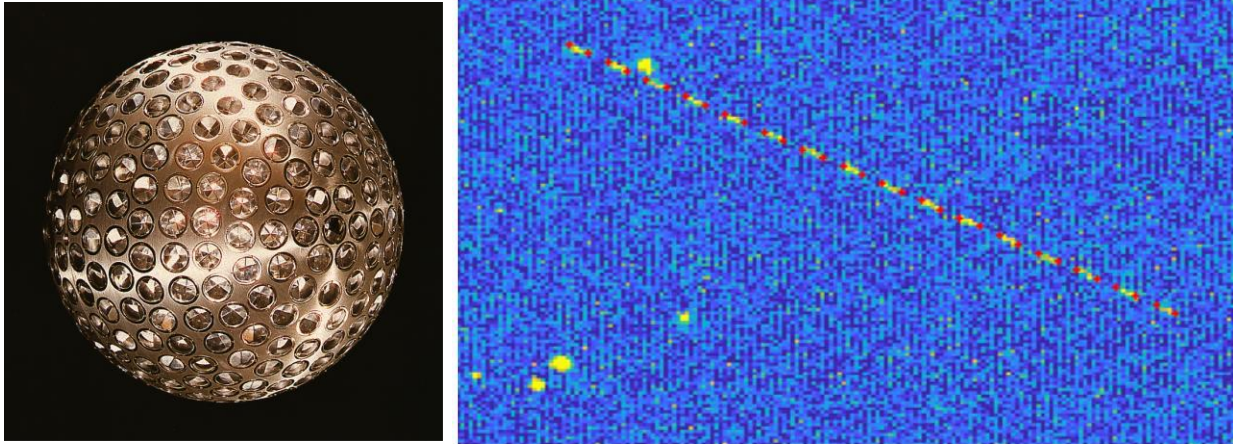


Figure 2 – LAGEOS 1 is pictured (left - credit: NASA) pre-launch and imaged by the detections system respectively. The picture shows that it is a shiny metal sphere with many corner cube reflectors. The image to the right shows 16 frames summed in an every-other fashion to show the individual tracks. Red crosses show the measured endpoints of each frame.

CALSPHERE 2 is smaller, a 0.355-m diameter bare aluminum sphere yielding a 0.099 m² projected area. For reference, the radar cross section is 0.045 m². The surface finish is not clear based on the descriptions available, nor from the few pictures that still exist, all of which appear to be the result of multiple generations of black and white copies.

From the measurements of all three of these objects, we can see that the standard model is underestimating the intensity. This is not so surprising given the objects, and we can see that CALSPHERE 2, which was launched in 1964, is still shiny.

Table 1 – This table summarizes the measurements of the three radar calibration satellites. The values shown are the average over all the observations of each object. CALSPHERE 2 was observed ten times, LAGEOS 1 was observed five times, and LAGEOS 2 was observed six times.

Name	NORAD	Area (m ²)	Range (km)	Phase (deg)	Model Est (mag)	Measured (mag)	Diff. (Δmag)
CALSPHERE 2	902	0.099	1320	68.5	10.28	8.68	-1.60
LAGEOS 1	8820	0.28	6047	64.9	12.71	11.58	-1.23
LAGEOS 2	22195	0.28	6105	56.6	12.58	12.23	-0.38

3.2. Cubesats

We observed four small cubesats: ExAlta-1, CUTE-1 CO-55, SEEDS-II, and NEE-02. Objects like this make excellent demonstrations of the sorts of targets that optical observations of LEO objects must be able to make routinely and robustly.

3.2.1. Exalta-1, a 3U Cubesat at 325 km

ExAlta-1 is a 3U cubesat launched from the International Space Station in 2017 into a 400 km altitude orbit. We observed it twice during one pass, where it moved at an apparent angular rate of 1.01 degrees per second. Figure 3 shows a sum image taken from the pass, demonstrating the rapid variation in intensity, along with images of the object at launch and pre-launch.

The first observations of ExAlta-1, shown as an image in Figure 3 and the extracted light curves in Figures 4 and 5, demonstrate that ExAlta-1 is tumbling with a period of 2.88 seconds, assuming that the three large peaks are each from different faces of the cubesat. An alternate hypothesis is that the period is 1.48 seconds, and that the first and last of the three large peaks are from the same side and that the very small blips, such as shown in Figure 5 are from the intervening faces. The rapid change in brightness shows that this observation caught a strong specular glint.

Unfortunately, the next observation, shown in Figure 6, didn't contain strong specular reflections, so we cannot confidently distinguish these two possible rotation rates. The speed with which ExAlta-1 transited through the field means that these light curves are sampled very well, with the object crossing slightly faster than 1000 pixels per second. The lines and points as plotted alternate in color with each different frame.

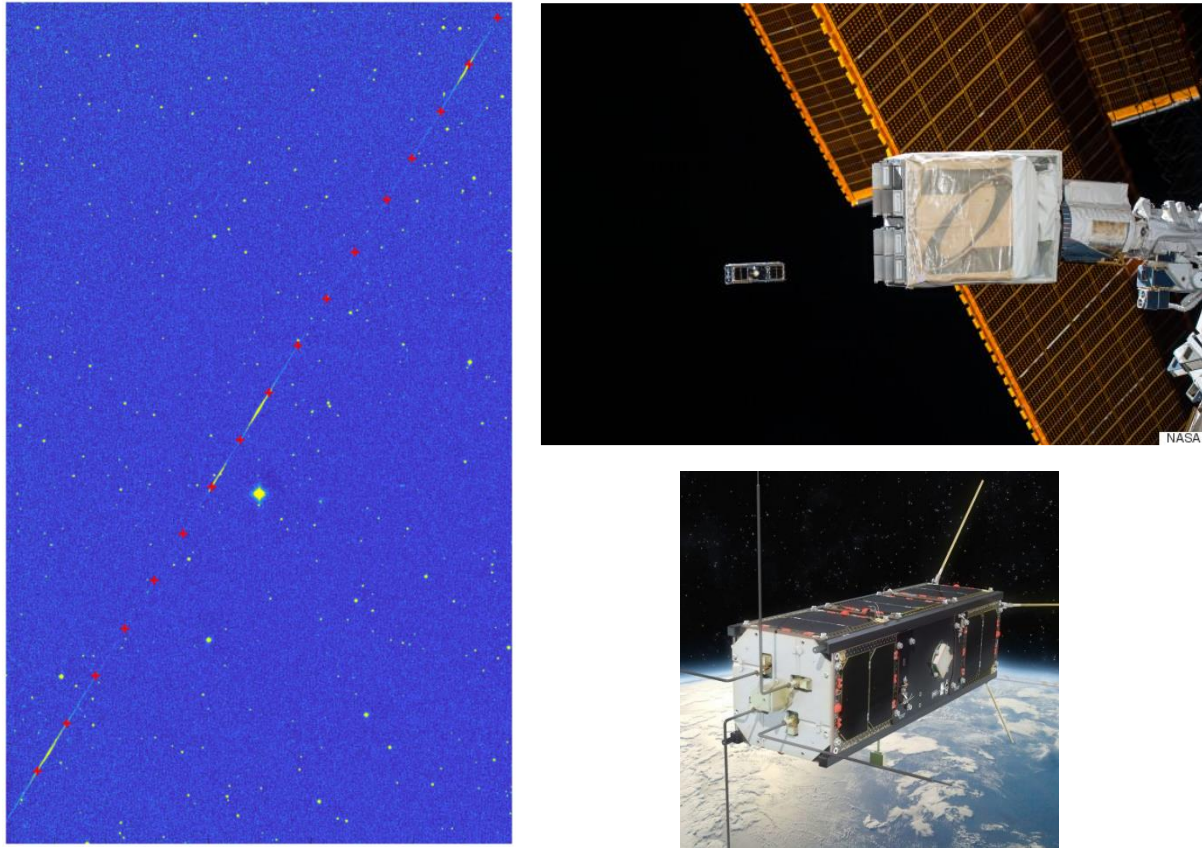


Figure 3 – The panel to the left shows the 3U cubesat ExAlta-1 as it passed through the FOV. This image is a sum of 20 of the 64 in the stack, which washes out the fainter parts of the signal but nicely demonstrates the rapidly varying signature. The resulting orbit altitude of 325 km causes it to appear to move at 3646 arcseconds per second, crossing the FOV in roughly two seconds. In each of the 20 frames, ExAlta-1 makes a 110-pixel-long streak and at times exceeds fifth magnitude, albeit only for a few milliseconds. The red crosses mark the extract endpoint positions of the object streak in each frame. The upper left panel (photo: NASA) shows a photo taken when ExAlta-1 was launched from the International Space Station. The lower right panel shows an image of ExAlta-1 (credit: University of Alberta) that depicts the extra antennae on it presumably as deployed, though we think the photo of the spacecraft was taken on the ground with the Earth image composited for public relations purposes.

Figure 6 shows the extracted light curves from the second image set taken of ExAlta-1. This set was taken approximately 40 seconds later and 40 degrees from the previous position, which is larger than the system usually exhibits between subsequent pointings, but a software setting led to a large step ahead of the object on its trajectory. At this point the large Sun glints had faded and the light curve behavior was less dramatic. The apparent rate is also almost half the previous, at 1870 arcseconds per second, at a range of 570 km. The two large peaks occur 2.88 seconds apart, which lends credit to the longer rotation period and the small intervening peaks might be from the beveled edges or antennae. In either case, it's clear that light curves such as these, taken over multiple passes, can clearly help understand optical signatures of cubesats.

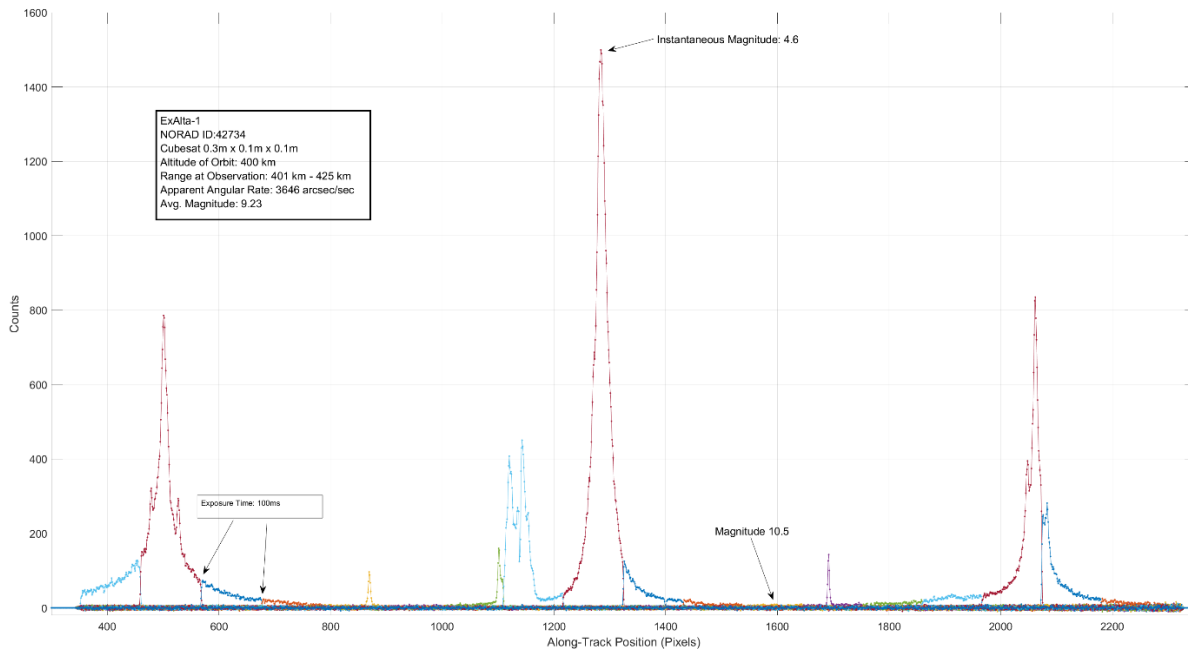


Figure 4 - The extracted light curve of Ex-Altia 1 is shown as it crossed the FOV. The different color lines and points are from separate subsequent 100-ms exposures and the time between each point is just under 1 ms. Light curves like this demonstrate how quickly the optical signature of LEO objects can change. If we assume that the peaks on the left and right sides of the plot represent opposite sides of a tumbling box, we obtain a rotation period of 3.8 seconds. The smaller bumps could be from the small metal antennae one Ex-Altia 1's corners. A Lambertian sphere radiometric model predicts that Ex-Altia 1 should be about magnitude 9.75 given its size, distance, and albedo of 0.16. Clearly this is a greatly simplified approximation given the observed values range from 10.5 to 4.6.

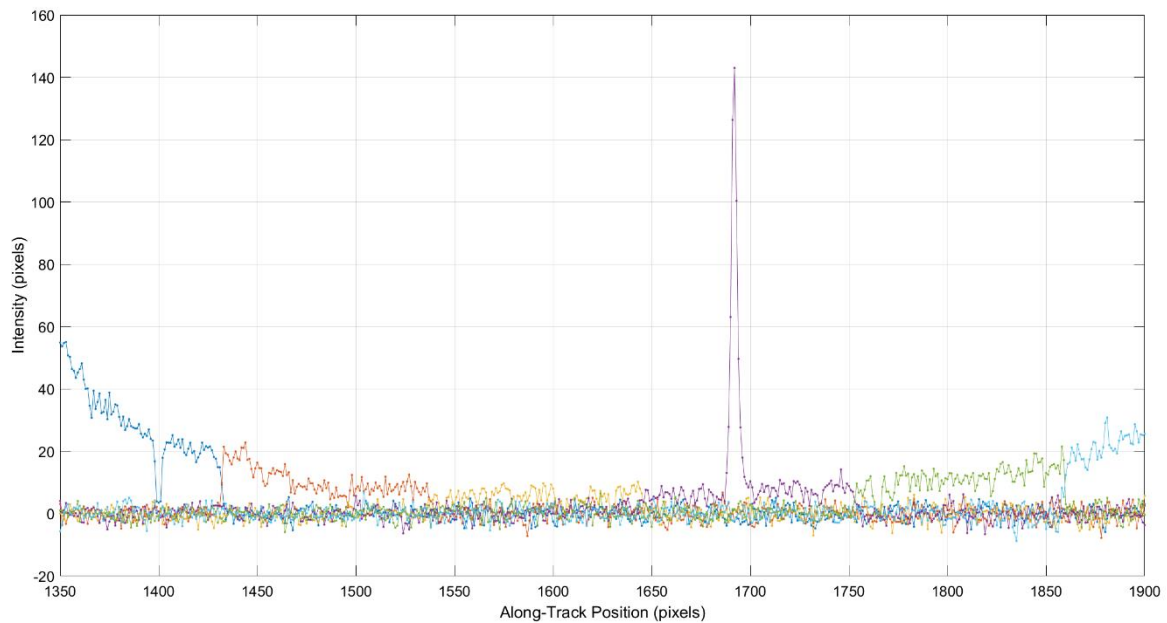


Figure 5 – These plots zoom in on the region of Figure 4 just to the right of the central peak and shows that even in the faintest parts of the light curve, where the instantaneous intensity is around magnitude 10.5, there is still visibly significant signal even at these short per-pixel dwell times.

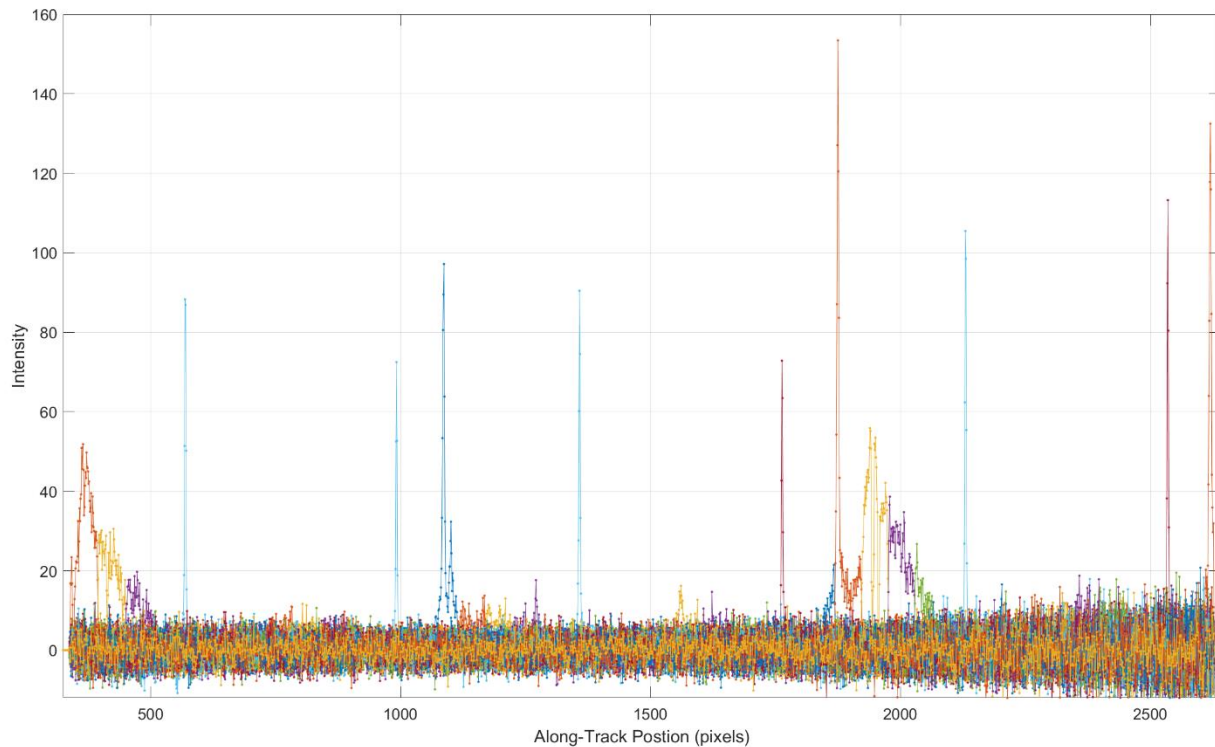


Figure 6 – The extracted light curve of ExAlta-1 taken roughly 40 seconds after that in Figure 4. The observation range is much larger here and the apparent angular velocity is about half that of the earlier figure. The two broad peaks are separated by 2.88 seconds, consistent with twice the time between the first and third peaks of Figure 4. The repetition of the first three skinnier peaks also recurs at this separation.

3.2.2. CUTE-1 CO-55

Figure 7 shows the light curve from one of the observations of the 1U cubesat CUTE-1 CO-55 which, in the data shown, is the canonical 1U cubesat at 1000km range. Our photometric model, using the corrected area based on the RCS of 0.08 m^2 , predicts this object should be roughly magnitude 10.5 while the measured values in this image set range from fainter than 12 to nearly 7. The other seven observations showed that CUTE-1 CO-55 typically ranged in the magnitude 12 to 13 range with other significant glints. More interesting is that in the image set immediately after the one shown in Figure 7, taken twelve seconds later, the object had dimmed to magnitude 15.4. It was still detected at a S/N of 11, but exactly what orientation of the object leads to that dramatic and long-lasting dimming is not clear. That detection is shown as in inset to Figure 7.

3.2.3. SEEDS-II

SEEDS-II is another 1U cubesat that was detected in five pointings. Figure 8 shows a relatively slowly changing light curve form when the object was at a range of 625 km. The photometric model estimates this object to be magnitude 9.8 given the range, phase and adjusted RCS. The measured values vary from 10 to 10.5 in the observations shown in the figure, to as faint as 14.5 in other observations.

3.2.4. NEE-02

NEE-02, also a 1U cubesat, at a range of 915 km, was a more challenging target. We detected it in three of seven observations with an intensity varying from magnitude 14.2 to 14.35. The latter detection is shown in the right panel of Figure 9. The non-detections exclude the object with magnitude upper limits in the 15.4-15.6 range. The panel to the left shows an image of NEE-02, which apparently has deployed solar panels that would normally cause a fairly significant optical signature. We can only conclude, from this and the other cubesat observations, that there are some very unfavorable orientations that lead to small effective optical cross-sections for these objects.

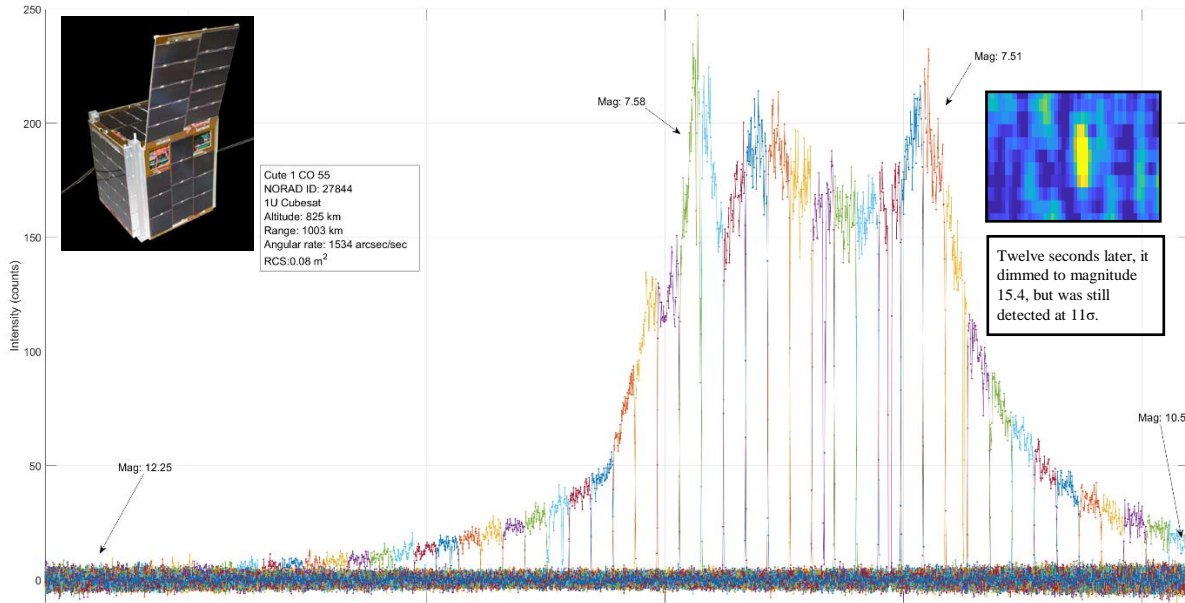


Figure 7 - The light curve of 1U Cubesat CUTE 1 CO-55 also shows dramatic variations. CUTE 1 was observed seven times and detected in six of the resulting data sets. In the set taken immediately after the one shown above it was detected at magnitude 15.4 (our faintest LEO yet!!!) with a significance of 11σ above the noise. In the image where it was not detected, we place an upper limit of magnitude 15.5, whereas the Lamertian model predicts 10.5 — a factor of 100! This case presents a nearly canonical configuration of a 1U Cubesat at 1000 km.

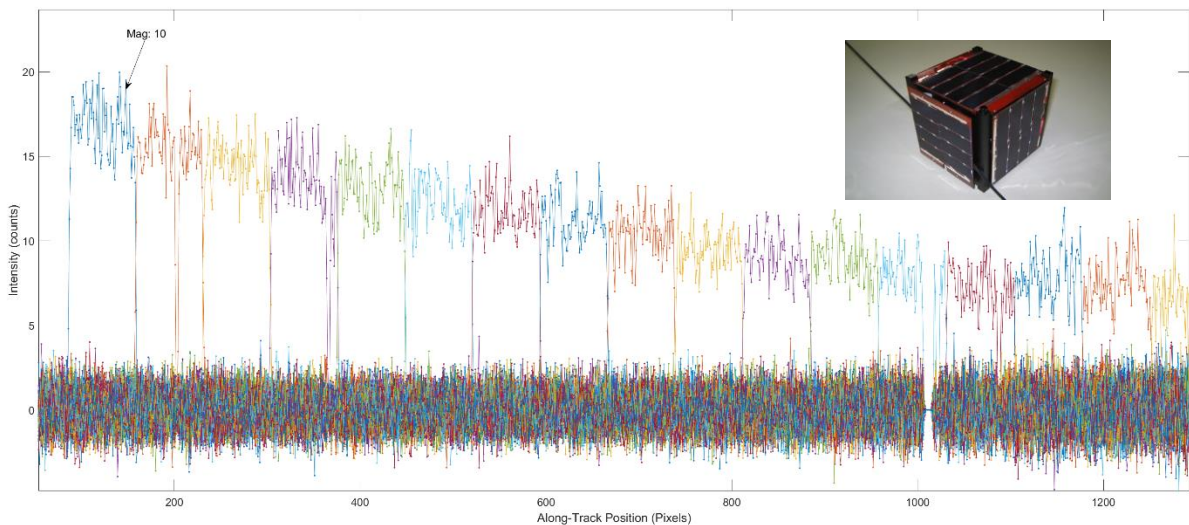
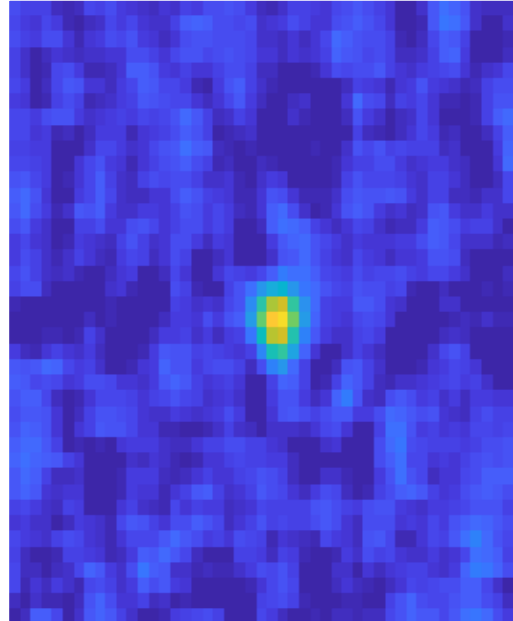


Figure 8 - A sample light curve of SEEDS-II, another 1U Cubesat that was successfully observed five times at a range of 625 km. Like the previous examples above, its measured intensity varied greatly from 10 to 14.5, whereas from its estimated size, range, and phase, one would expect magnitude 9.8. A pre-launch image of SEEDS-II is shown in the inset.



Figure 9 - NEE-02 was measured in three of seven observations, ranging from 14.2 to 14.35, the latter detection is shown in the image to the right. The non-detections placed upper limits of 15.4-15.6. This 1U Cubesat was 915 km away at the time of measurement.



3.3. Fengyun 1C (FY) Debris

At any given time, over any observing site, the plurality of known objects moving overhead is debris from the 2007 FY antisatellite missile test [18]. FY debris represent a relevant and challenging test for optical LEO observations. Although radar cross-sections are publicly available for most of these objects, very little is known about their size, shape, material, color, or orientation. We attempted 50 observations of FY debris spread over nine objects. Three objects were detected, and upper limits placed on the rest. The difference between the upper limits and expected values are large. Either they are much blacker than expected, smaller than reported by RCS, or the TLE positions very much in error. Each of these potential explanations have interesting implications.

3.3.1. Detected FY Debris

Table 2 summarizes the measurements of FY debris for the three detected objects. The range and illumination phase are calculated from the TLE positions, and the model value is the estimated diffuse Lambertian model discussed earlier. The measured intensity and associated error, based on the measured variance, are the sum for the entire image set, which for these objects is approximately four seconds. These reported errors do not include the effects of scintillation, which will dominate the sky, shot, and detector noise, even on several-second timescales for telescopes of this size, especially in the cases where the object is being observed at large-slant ranges.

Figure 10 shows a sum of every frame from the observations of FY Debris 29918, which has the largest RCS, 0.08m^2 , of the sample. This piece is very nearly as bright as the model predicts, near magnitude 10. Figure 11 shows the extracted light curve during the same period as Figure 10, with a very strong and consistent signal.

Figure 12 shows a sample light curve from a single frame for FY Debris 29796, which has an RCS of 0.044 m². It is much fainter, though, than the RCS difference would imply. The model predictions range from magnitude 10.8 to 11.1, but the measured values are around 2.5 magnitudes fainter. Although this might be because of errors in the reported RCS value, a consistent factor of 10 is not trivial to explain and may indicate a much less reflective surface.

The remaining detected FY Debris 30920 has the smallest RCS of the all nine: 0.0084 m². Its measured intensity varied from magnitude 13.6 to 14.2, around 1.5 magnitudes fainter than expected.

Table 2 – This table summarizes the measurements of the three detected FY debris objects. The values shown are the average over each image set.

Observation Time:	Range	Phase	Model	Measured	Meas. Err	S/N	Diff.
	(km)	(deg)	(mag)	(mag)	(±mag)		(mag)
29796 (RCS = 0.044 m²)							
2018-01-14T01:22:30.095	978.74	76.18	11.01	13.58	0.025	40.4	2.56
2018-01-14T01:22:47.102	934.30	76.05	10.91	13.46	0.022	44.8	2.55
2018-01-14T01:23:21.106	888.64	75.80	10.79	13.48	0.023	43.5	2.69
2018-01-14T01:23:38.291	889.75	75.68	10.79	13.40	0.022	45.7	2.61
2018-01-14T01:23:55.120	906.77	75.57	10.83	13.37	0.023	44.0	2.54
2018-01-14T01:24:12.088	939.03	75.45	10.91	13.41	0.024	41.2	2.50
2018-01-14T01:24:29.113	985.12	75.34	11.01	13.34	0.024	40.9	2.33
2018-01-14T01:24:46.657	1045.07	75.24	11.13	13.33	0.024	41.3	2.20
29918 (RCS = 0.08 m²)							
2018-01-14T12:55:39.097	883.80	70.39	10.01	9.83	0.001	1053	-0.18
2018-01-14T12:55:59.111	858.93	70.45	9.95	9.76	0.001	1085	-0.19
2018-01-14T12:56:19.098	857.01	70.52	9.95	9.79	0.001	982	-0.15
2018-01-14T12:56:39.078	878.14	70.60	10.00	9.98	0.001	901	-0.02
2018-01-14T12:56:59.107	920.84	70.68	10.11	10.12	0.001	773	0.01
30920 (RCS = 0.0084 m²)							
2018-01-15T01:44:01.089	845.51	68.04	12.24	13.64	0.027	36.4	1.40
2018-01-15T01:44:25.119	858.04	68.61	12.28	13.95	0.028	35.5	1.67
2018-01-15T01:44:49.110	903.52	69.19	12.41	14.17	0.032	31.5	1.77
2018-01-15T01:45:13.087	977.30	69.78	12.59	14.20	0.032	31.1	1.61

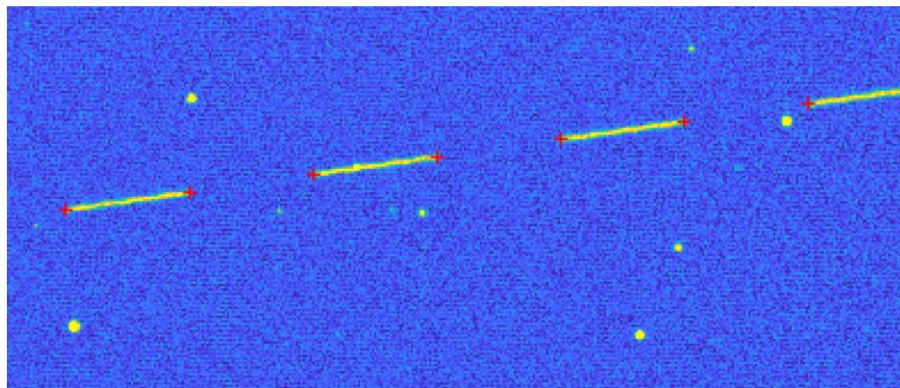


Figure 10 - Sample images (every other exposure) are shown in sum for FY Debris 29918, the brightest of those detected in this work.

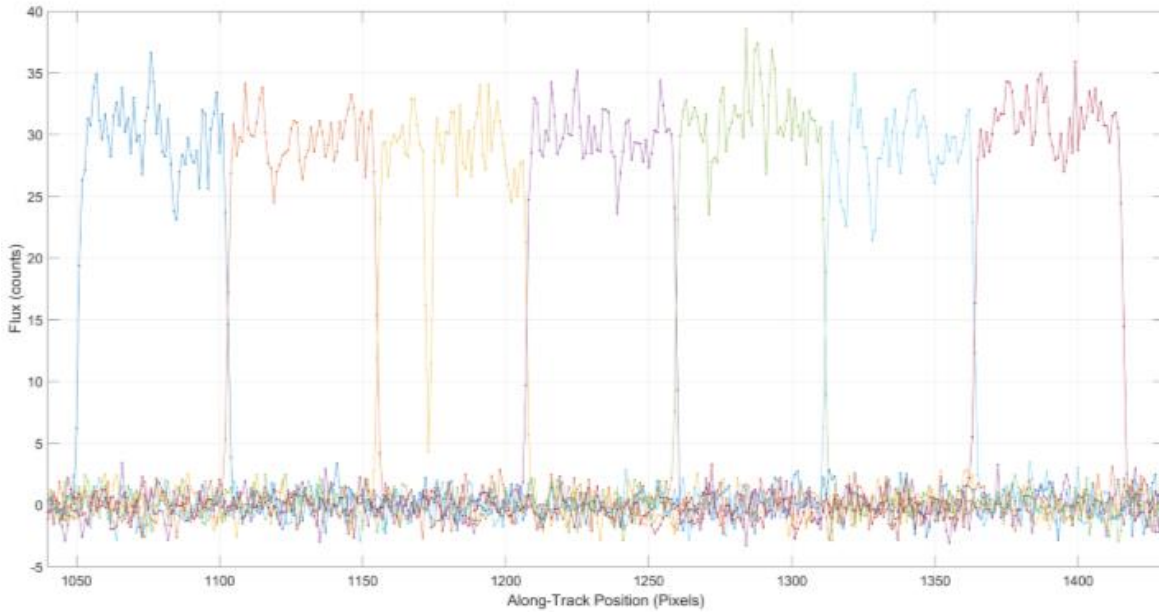


Figure 11 - The resulting light curve for the observations shown in Figure 10, except with all the exposures included.

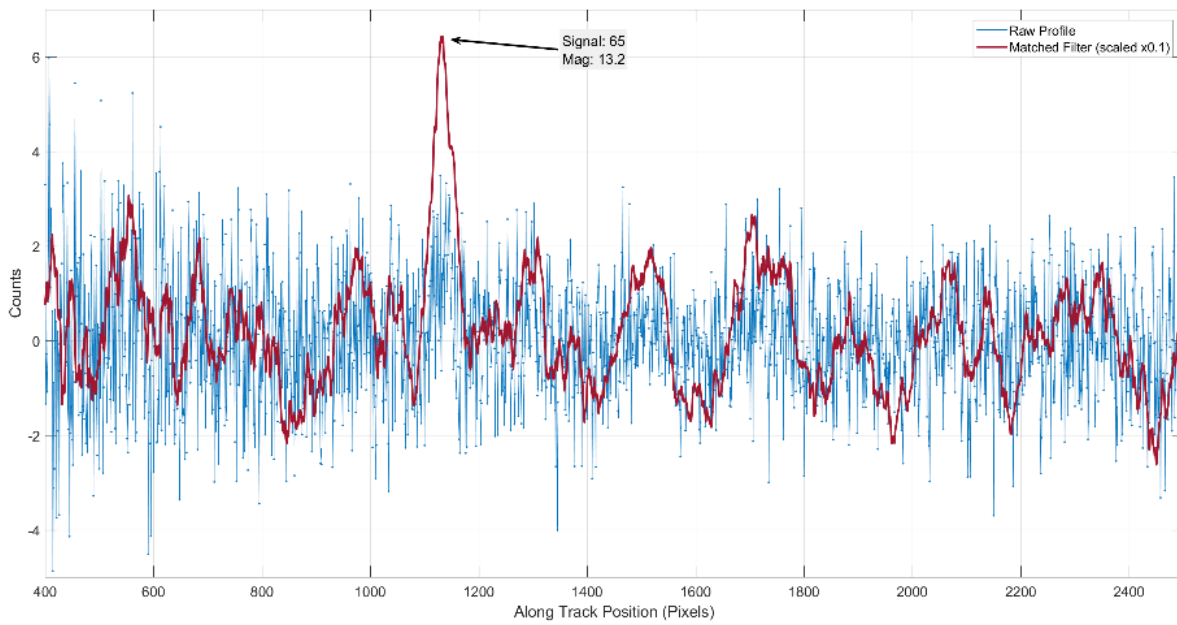


Figure 12 - A sample extract light curve from FY Debris 29796 showing a noisy but significant detection. The blue line is the raw extracted light curve, and the red line is an expected velocity-matched filter applied to it, which is shown scaled down by a factor of 10. In this representation this may appear a marginal detection, but for the entire pass through the FOV, it has a S/N of >40.

3.3.2 Non-detections

Six of the nine FY debris objects we targeted were not successfully detected. Because we measure the noise using the image set, we can place upper limits on a six sigma detection and convert that into a GAIA-referenced magnitude based on the star calibration. Most of the upper limit exclusions are fainter than 15th magnitude, which is of the order three magnitudes fainter than expected. The system FOV is so large that we can largely eliminate normal TLE errors as the cause. The TLEs generated after the observations for these objects do not show the objects shifted more than a few kilometers from the observation epoch TLE, even then the shifts are mostly in the along-track direction. We have numerous frames in front and behind the expected trajectory so we can exclude 20+ km along track errors in each direction. Cross-track we can exclude regions within 10 km, which is considerably larger than the usual expected TLE errors of a few km.

Some very interesting suggestions were made during the poster session where this was presented to explain these non-detections at such faint limits. The most interesting posed that most of what is known of material properties of spacecraft and debris is largely based on the exteriors of the objects. Because FY debris was the product of a catastrophic explosion, that prior distribution may not apply. The insides of space optical systems are painted black. Spacecraft structures can use carbon fiber composites which, when fragmented, are black. Combustion residue products are often black carbon. We feel that these explanations are plausible, but still would be rather coincidental if they just happened to apply to 6 of 9 random pieces of the FY spacecraft.

NORAD ID	RCS	Range	Model Est.	Detection U.L.	Exclusion Along Track	Exclusion X-Track	Num Obs.
	(m²)	(km)	(mag)	(mag)	(km)	(km)	
37428	0.0129	966	12.1 - 12.5	> 15.5	±25	±15	4
31658	0.0128	1130	12.6 - 13.1	> 15.2	±29	±19	9
29775	0.032	760	10.4 - 10.8	> 15.1	±20	±12	2
30856	0.012	1140	12.1 - 12.4	> 15.3	±29	±19	9
31360	0.014	857	11.9 - 12.1	> 14.8	±22	±14	5
36170	0.01	856	12.3 - 12.5	> 15.4	±22	±14	3

4. ONGOING EXPERIMENTS

These observations demonstrate the potential for small telescopes to contribute substantial and robust measurements of small cubesats and debris in LEO. Known satellites and larger debris can be precisely and accurately measured and monitored, with well-sampled light curves on millisecond timescales. Smaller debris pieces can be localized and average intensity measured below 15th magnitude, a level only previously achievable on small telescopes with photon-counting detectors. A large fraction of the debris was not detected and only intense observing campaigns will help understand why.

We continue to adapt our techniques to allow systems like these to be in operation in the next few months, at which point a catalog of optical measurements can begin. Comprehensive coverage of LEO will require many such systems, but because they are relatively inexpensive and based largely on commercial components, rapid and global deployment is feasible. Moreover, these systems use the same techniques as our blind/uncued search, so the only thing limiting that capability is additional on-site computing. And, between dusk and dawn twilight, these systems are potent instruments for GEO surveillance as well.

REFERENCES

- [1] C. E. Livingstone, “Radar systems for monitoring objects in geosynchronous orbit,” Defence Research and Development Canada, DRDC Ottawa TR 2013-009, 2013.
- [2] D. Mehrholz, “Radar Observations of Geosynchronous Orbits,” in *Second European Conference on Space Debris*, 1997, vol. 393, p. 51.
- [3] L. Rodriguez, G. Krier, M. Thill, and J. de Vicente, *Passive Ranging for Geostationary Satellites: On a Novel System and Operational Benefits*. 2014.
- [4] R. Jedicke, J. Larsen, and T. Spahr, “Observational selection effects in asteroid surveys,” in *In Asteroids III (W.F. Bottke, A. Cellino. P. Paolicchi and R.P. Binzel, Eds, 2002, pp. 71–88.*
- [5] J. T. McGraw, P. C. Zimmer, and M. R. Ackermann, “Ever Wonder What’s in Molniya? We do.,” in *Advanced Maui Optical and Space Surveillance (AMOS) Technologies Conference*, 2017, p. 107.
- [6] P. Zimmer, J. McGraw, and M. Ackermann, “Real-Time Optical Surveillance of LEO/MEO with Small Telescopes,” in *Advanced Maui Optical and Space Surveillance Technologies Conference*, 2015, p. 103.
- [7] J. McGraw, P. Zimmer, and M. Ackermann, “Multiple Observing Modes for Wide-field Optical Surveillance of GEO Space,” in *Advanced Maui Optical and Space Surveillance Technologies Conference*, 2016, p. 24.
- [8] M. Ackermann, D. Cox, J. McGraw, and P. Zimmer, “Lens and Camera Arrays for Sky Surveys and Space Surveillance,” in *Advanced Maui Optical and Space Surveillance Technologies Conference*, 2016, p. 58.
- [9] P. Zimmer, J. T. McGraw, and M. R. Ackermann, “Towards Routine Uncued Surveillance of Small Objects at and near Geostationary Orbit with Small Telescopes,” in *Advanced Maui Optical and Space Surveillance (AMOS) Technologies Conference*, 2017, p. 30.
- [10] Gaia Collaboration *et al.*, “The Gaia mission,” *Astron. Astrophys.*, vol. 595, p. A1, Nov. 2016.
- [11] Gaia Collaboration *et al.*, “Gaia Data Release 1. Testing parallaxes with local Cepheids and RR Lyrae stars,” *Astron. Astrophys.*, vol. 605, p. A79, Sep. 2017.
- [12] J. Shell, “Optimizing orbital debris monitoring with optical telescopes,” in *Advanced Maui Optical and Space Surveillance Technologies Conference*, 2010, p. E42.
- [13] W. E. Krag, “Visible magnitude of typical satellites in synchronous orbits,” *NASA STIRecon Tech. Rep. N*, vol. 75, Sep. 1974.
- [14] L. Casagrande and D. A. Vandenberg, “On the use of Gaia magnitudes and new tables of bolometric corrections,” *Mon. Not. R. Astron. Soc.*, vol. 479, pp. L102–L107, Sep. 2018.
- [15] D. K. Barton, D. R. Brillinger, A. El-Shaarawi, P. McDaniel, K. H. Pollock, and M. Tuley, “Final Report of the Haystack Orbital Debris Data Review Panel,” 1998.
- [16] R. Lambour, T. Morgan, and N. Rajan, “Orbital debris size estimation from radar cross section measurements,” in *Proceeding of the 2000 Space Control Conference*, 2000.
- [17] M. Mulrooney, M. Matney, M. Hejduk, and E. Barker, “An Investigation of Global Albedo Values,” in *Advanced Maui Optical and Space Surveillance Technologies Conference*, 2008, p. E65.
- [18] B. Weeden and V. Samson, “Global Counterspace Capabilities: An Open Source Assessment,” *Secure World Found.*, pp. 3–14, 2018.